iScience

CellPress
OPEN ACCESS

Article

The concerted proton-electron transfer mechanism of proton migration in the electrochemical interface

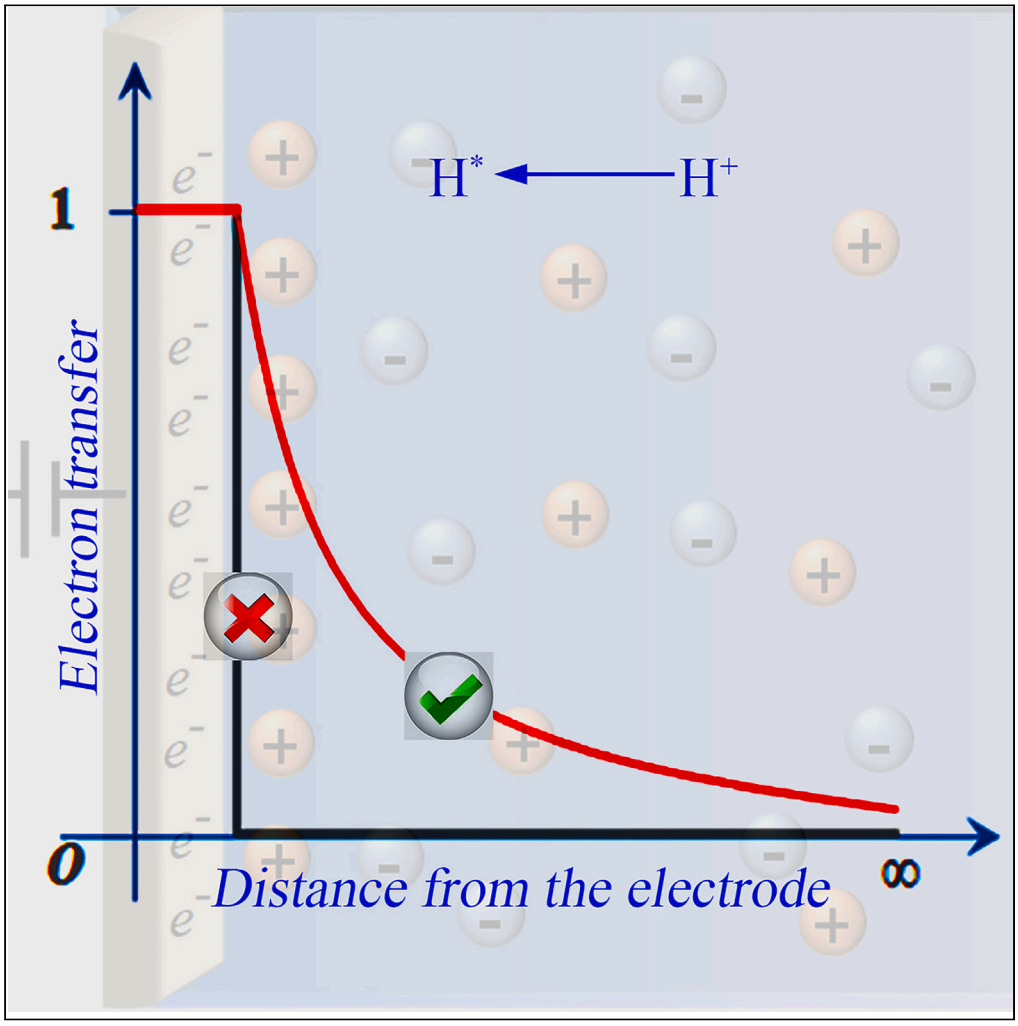

Guoping Gao, Lin-Wang Wang

guopinggao@xjtu.edu.cn (G.G.)
lwwang@semi.ac.cn (L.-W.W.)

Highlights

The proton migration goes through the concerted proton-electron transfer mechanism

The quantity of electron transfer is inversely proportional to the distance

The dissipated electrical energy induces the proton's accumulation near the electrode

The proton migration is an essential component of the electrochemical reaction

Gao & Wang, iScience *26*, 108318
November 17, 2023 © 2023 The Author(s).
https://doi.org/10.1016/j.isci.2023.108318

iScience

CellPress
OPEN ACCESS

Article

The concerted proton-electron transfer mechanism of proton migration in the electrochemical interface

Guoping Gao[1,3,*] and Lin-Wang Wang[2,*]

SUMMARY

The proton migration in the electrochemical interface is a fundamental electrochemical processes in proton involved reactions. We find fractional electron transfer, which is inversely proportional to the distance between the proton and electrode, during the proton migration under constant potential. The electrical energy carried by the transferred charge facilitates the proton to overcome the chemical barrier in the migration pathway, which is accounting for more than half electrical energy in the proton involved reactions. Consequently, less charge transfer and energy exchange take place in the reduction process. Therefore, the proton migration in the electrochemical interface is an essential component of the electrochemical reaction in terms of electron transfer and energy conversation, and are worthy of more attention in the rational design and optimization of electrochemical systems.

INTRODUCTION

Proton, the simplest cation, participates in numerous significant electrochemical energy conversion reactions, including water splitting,[1] CO_2 reduction,[2] and N_2 reduction.[3] It carries out the tasks of mass transport and energy transfer in these electrochemical reactions. The proton must go through two processes in order to accomplish these tasks: migration from the outer Helmholtz layers to the inner Helmholtz layers and reduction process on the electrode surface.

It is widely assumed that charge transfer and energy exchange primarily take place in the reduction process,[4,5] and the reduction process is considered as the primary process in the electrochemical reactions. Hence, there have been significant attempts to improve the catalytic performance of electrode.[6,7] Based on the supposition that there is no charge transfer involved in the proton migration process, sequential proton transfer electron transfer mechanism, much less focus is placed on comprehending the proton migration process. Some recent studies point out that solvated protons in the first water layer outside a metal surface have fractional charges,[1,8] but those in the third water layer have charges close to $1e^+$.[9] It is unclear what causes this fractional charge, how proton and electron transfer interact, or how this affects the energetics of the proton migration. Investigating the interdependence of proton and electron transfer and the associated energetics will shed new light on many electrochemical reactions. However, it is a challenge for conventional density functional theory (DFT) calculations based on the fixed charge method to describe chemical processes involving electron transfer.[10,11] Thus, a grand canonical DFT method that allows the total charge to fluctuate during the calculation holds substantial advantages in investigating such critical electrochemical processes.[12–16]

In this work, we examine the migration of protons in the electrical double layer and the reduction reaction on the Pt (111) surface using the grand canonical fixed-potential method. This method adjusts the total number of electrons to satisfy the fixed potential (Fermi energy) of the electrode as shown in Figure 1. We track the total overall energy and electron of the entire system during the proton migration from the water layers to Pt (111) under constant potential. By doing so, we learn how the simulated system and the external reservoir exchange electrons and energy throughout the proton migration. Additionally, the impact of the electrode potential on the proton migration is determined by repeating the previous calculation under various constant potentials.

RESULTS

To verify the reliability of the electrical double layer model, an excess proton in each first water layer outside the two Pt (111) surfaces under an absolute potential of −4.44 V, which represents protons in the inner Helmholtz layer, is used as an example to illustrate the hydrogen reduction environment of the electrical double layer. We divided the XY plane-integrated electron density into the Pt electrode zone (in green) and protonated water layers zone (in blue) via the charge density minima point between them as shown in Figure 2A. Subtracting integration electrons in each zone by their valence electrons, respectively, we can calculate the charge state of the electrode and protonated water layers.

[1]MOE Key Laboratory for Non-equilibrium Synthesis and Modulation of Condensed Matter, Shaanxi Province Key Laboratory of Advanced Functional Materials and Mesoscopic Physics, School of Physics, Xi'an Jiaotong University, Xi'an, Shaanxi 710049, China
[2]State Key Laboratory of Superlattices and Microstructures, Institute of Semiconductors, Chinese Academy of Sciences, Beijing 100083, China
[3]Lead contact
*Correspondence: guopinggao@xjtu.edu.cn (G.G.), lwwang@semi.ac.cn (L.-W.W.)
https://doi.org/10.1016/j.isci.2023.108318

This is an open access article under the CC BY-NC-ND license (http://creativecommons.org/licenses/by-nc-nd/4.0/).

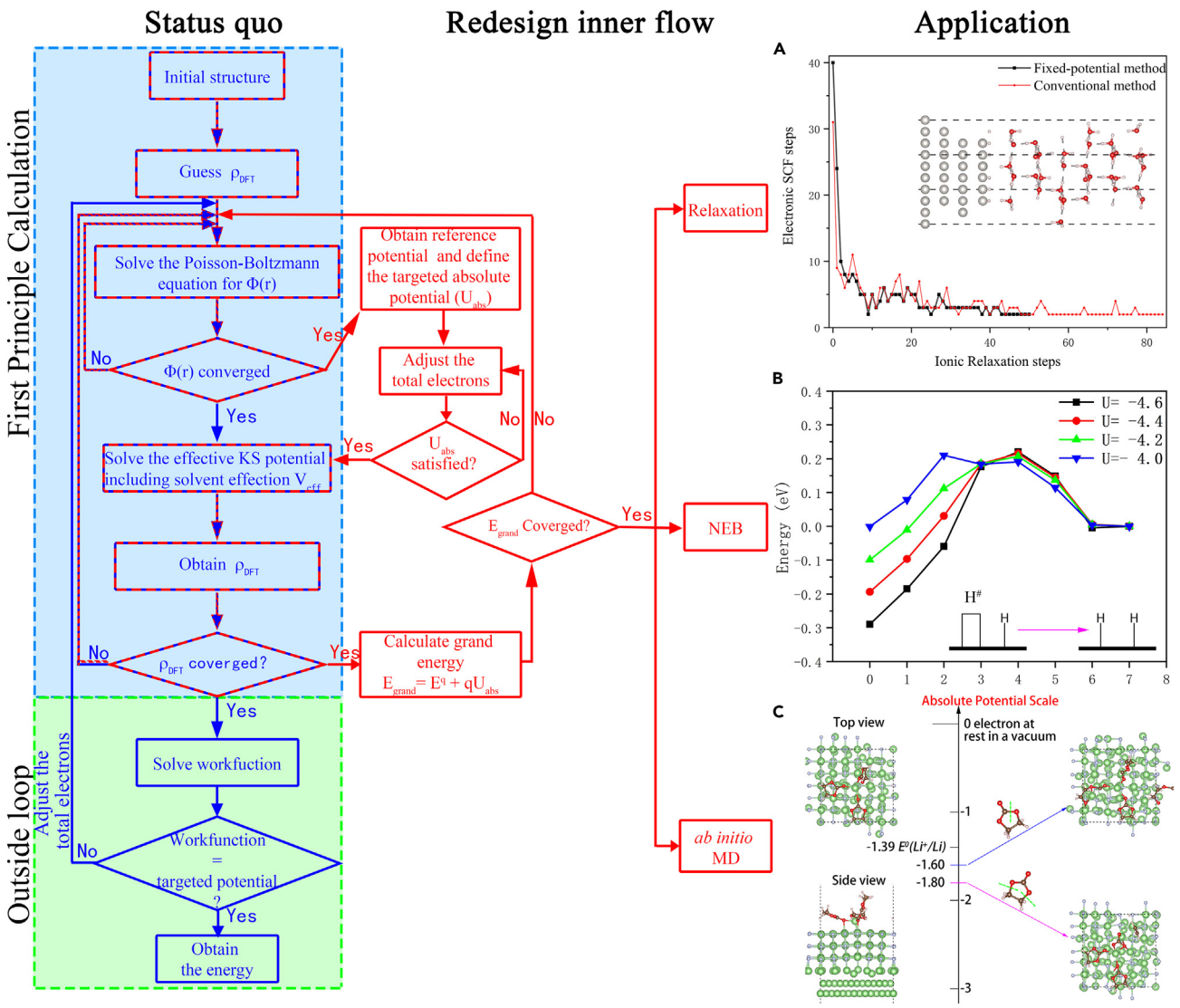

Figure 1. The Fixed-potential method

The flow of the fixed-potential method realized by the outside loop is present in blue color, while the fixed-potential method designed in our group is highlighted in red color.

(A) the comparison of the calculated performance of the fixed-potential method and conventional DFT method; (B) the fixed-potential method for NEB calculations of the Volmer reaction in hydrogen evolution reaction; (C) the fixed-potential method for *ab initio* MD to simulate the ethylene carbonate decomposition.

Under an absolute potential of −4.44 V, the charge state of the entire system is 0.23 e^+. Specifically, the charge state of the electrode is 1.31e^-, while each protonated water-layers has a charge state of 0.77e^+. The opposite charges at the solid-solvent interface generate a local electric field directed toward the electrode and an electrostatic potential drop within the electrical double layer. Similar results can be found when the proton is in the other water layer, as shown in Table S1 in the supplemental information.

The electrostatic potential drop in the solid-solvent interface is another physical characteristic used to evaluate the electrical double layer model. In plane-wave pseudopotential DFT calculations, the Columbia potential includes the Hartree potential and the local part of the pseudopotential is shown in Figure 2C via dashed-dotted green line,[17] which exhibits deep wells at each nucleus plane. Systems with random ion positions are expected to smooth the deep well oscillations. However, it is still a challenge to obtain an accurate electrostatic potential via this approach.[18] A rough alignment of the electrostatic potential based on the highest occupied molecular orbital (HOMO) of the electrode and solvent is an appropriate compromise. In our fixed-potential method, a linearized Poisson-Boltzmann equation[19] is used to screen the ions' electrostatic potential exponentially in the implicit solvent zone and provide a converged flat potential far away from the surface where the electron density is zero. The flat potential is set as the absolute potential of zero. By doing that, the energy of electrons in a vacuum just

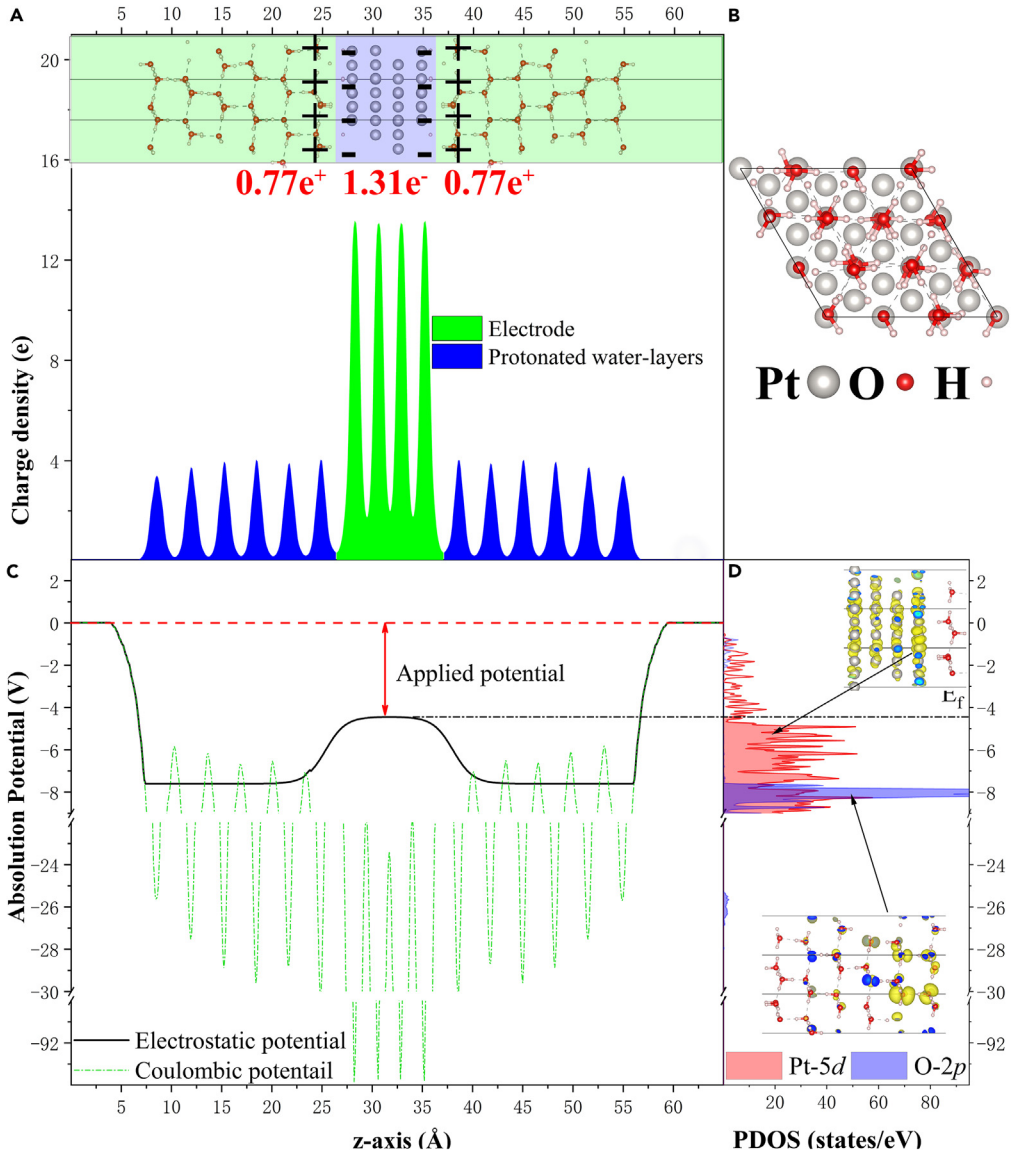

Figure 2. Model of the electrical double layer

The side view (A) and top view (B) of a proton in the first water layer outside the Pt (111) surface; plane-integrated electron density distribution as a function of the z-coordinate (A); the Coulombic potential and the alignment of the electrostatic potential as a function of the z-coordinate (C); the PDOS and the HOMO orbitals of the Pt-d and O-p orbitals (D).

outside the solvent becomes the reference for the fixed potential of the electrode.[20] In this example, the absolute electrode potential of the electrode is fixed at −4.44 V (the standard hydrogen electrode level). The system's density of states at −4.44 V is mainly occupied by the 5*d* orbitals of Pt (111), while the HOMO of the protonated water layers featured by the O-2*p* orbitals is approximately at −7.30 V as shown in Figure 2D, which is close to the energy level HOMO of water and protonated water (See Figure S1 supplemental information). The negatively charged electrode and positively charged protonated water layer will generate an electrostatic potential drop at the boundary of the Pt electrode and water solvent (~26 Å and ~35 Å on the z axis), which connects the electrostatic potential gap between the Pt electrode and water solvent. Therefore, the aligned electrostatic potential is −4.44 V in the Pt electrode and then decreases gradually at the solid-solvent interface to −7.30 V till the outer Helmholtz water layers. According to the aforementioned analysis, the electrical double layer model can efficiently capture the key characteristic of the electrical double layer and reproduce the hydrogen reduction environment.

In the following, we track the adiabatic electron transfer process during the proton migration and reduction process in the Volmer reaction under constant potential (−4.44 V) as present in Figure 3A. If we set the total electrons of the system with the proton in the sixth water layer (N_e^{6th}) as the reference, the quantity of adiabatic charge transfer is defined as the extra charge flowing from the reservoir to the system during

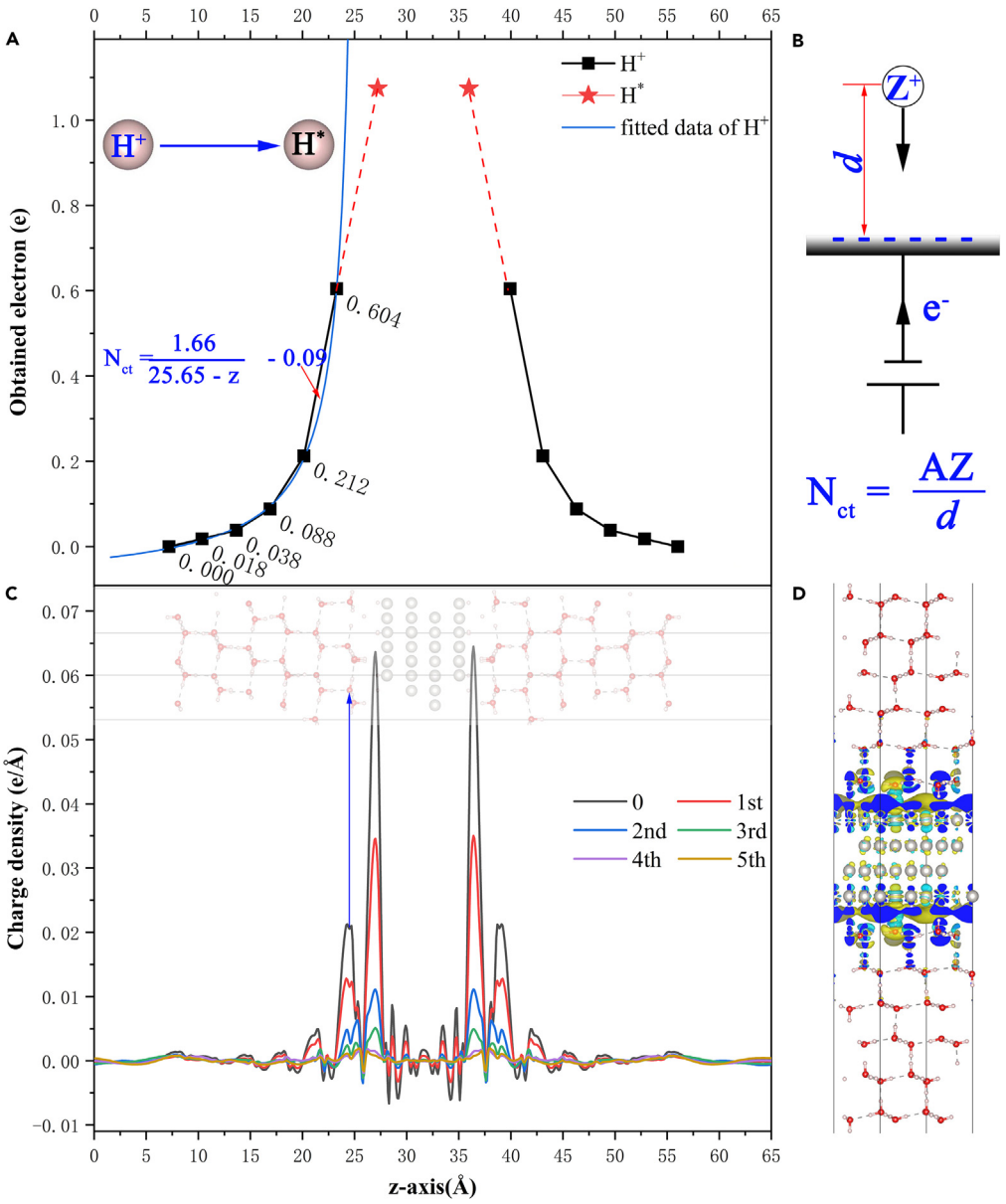

Figure 3. The electron evolution during proton migration and reduction under the constant potential of −4.44V

(A) The charge transfer of the whole system during the proton migration from the outer Helmholtz layer to the Pt electrode under different potentials. The detailed data can be seen in Table S2 in the supplemental information; (B) the sketch of proton migration to the electrode; (C) the charge density difference (Δ ρ) caused by the proton migration; (D) plots of 3D differential charge densities between protons at the 6th and 1st water layer ($\Delta\rho = (\rho_{0th} - \rho^0_{0th}) - (\rho_{6th} - \rho^0_{6th})$) at isosurfaces of 0.00065 e/Å^3 (yellow, charge accumulation) and - 0.00065 e/Å^3 (blue, charge depletion).

the proton migration from the outer to inner Helmholtz layers under constant potential. Therefore, the quantity of adiabatic charge transfer (N_{ct}) is calculated by Equation 1:

$$N_{ct} = N_e^{xth} - N_e^{6th} \quad \text{(Equation 1)}$$

Here, the N_e^{xth} is total electron when the proton at xth water layer. The N_{ct} rises to 0.018e$^-$, 0.038e$^-$, 0.088e$^-$, 0.212e$^-$, and 0.604e$^-$ when the proton migrates into the 5th, 4th, 3rd, 2nd, and 1st water layers, respectively. The N_{ct} can be fitted by a formula as the function of the proton's z-coordination (z): $N_{ct} = \frac{1.66}{25.65 - z} - 0.09$. The fitted parameter of 25.65 is slightly smaller than the top Pt nucleus layer's z-coordination (28.12 Å). Screened by their valence electrons and terminated H*, the effective electrode surface is slightly outside of the Pt nucleus layers. Thus, 25.65 Å represents the position of the effective electrode surface, and z-25.65 is the proton's distance (d) from the electrode. The valence of the proton

($Z,1e^+$) multiplied by a factor (A) is responsible for the 1.66. The A is expected to relate to the permittivity of the solvent, the orientation of the solvent and the states of the electrode. The determination of the A is beyond the scope of this work. In addition, the 0.09 is nearly zero and negligible, which can be attributed to the uncertainty in electron calculation. Therefore, the fitted formula can be condensed into Equation 2 and illustrated in Figure 3B:

$$N_{ct} = -\frac{AZ}{d} \quad \text{(Equation 2)}$$

Based on the formula, the adiabatic electron transfers from the reservoir to the electrode during the proton migration to maintain the potential of the electrode. The quantity of the adiabatic charge transfer is proportional to the valence of the protons and inversely proportional to its distance from the electrode as presented in Figure 3B. In addition, similar adiabatic charge transfer behaviors can be observed under different applied potentials (See Figure S5, supplemental information) and under various H* coverages and with other ions involved (Na^+ and Cl^-, See Figures S3, S4, and S6, supplemental information). Therefore, the proton migration goes through the concerted proton-electron transfer mechanism.

The observed results, however, depart from the induced charge of the point-infinite-plate obtained by the image method, where the induced charge is independent of the distance z under the assumption that the dielectric constant of water is a constant. As we know, the electric field induced by the proton is proportional to $\frac{Q}{d^2}$, where Q is the proton's charge. The local electric field induced by the proton is greater than 10^8 V/m within a range of 10 Å. In such extremely high electric fields, the water solvent will become dipolar saturated resulting in a field-induced reduction in the dielectric constant.[21,22] The field-induced reduction in the dielectric constant results in the enhancement of the electric field pointed toward the Pt surface during the proton migration, and more induced/compensation charge is required to maintain the constant potential. Therefore, the charge transfer is caused by the reduction of the effective dielectric constant as the proton approaches the electrode.

To finish the whole Volmer reaction, the proton will migrate further toward the Pt (111) surface (the reduction process). The electron obtained during the reduction process (defined as the reduction charge, N_{rc}), is only 0.47 e^-, which conflicts with the common assumption that the reduction charge is mainly obtained in the reduction process. The N_{ic} and N_{rc} make up the obtained electron of the Volmer reaction (N_{oe}). The N_{oe} (1.07 e^-) is not exactly 1.0 e^- as the proton's chemisorption alters the electrode's work function and surface dipoles slightly. Generally, the larger the work function of a system, the harder it is to lose electrons and the easier it is to trap electrons under the applied potential. The work function Φ is strongly associated with the electronegativity χ. In our calculations, the work function can be obtained directly from the absolute potential of zero-charge (PZC), i.e., $\Phi = -eU_{PZC}$. As a result, the calculated Φ of * (H coverage of 5/9) and H* (H coverage of 6/9) are 5.11 and 5.14 eV, respectively. Additionally, the surface dipole moment d can be given by the work function change $\Delta\Phi$, i.e., Helmholtz equation $d = -\varepsilon_0 A_{surf}\Delta\Phi/e$, where the A_{surf} is the surface area of the catalyst and ε_0 is the vacuum permittivity. The dipole moment of H* is −0.03 Debye. A negative dipole moment d indicates a dipole pointing to the catalyst surface, resulting in an increase in the work function and making it easier to gain electrons from the reservoir. Therefore, the H* will have a lower charge state than the * and experience more than one electron transfer during the Volmer reaction. The charge transfer during the element reaction will deviate from the integer slightly as the intermediate states alter the work function and dipole. It is worth noting this work function altering does not change the total number of electrons involved in the entire redox reaction.[10]

It is a challenge to locate the N_{ct} of the proton migration since the N_{ct} is less than 0.60 e^- whereas the system's total electron is approximately 1236 e^-. To address this issue, we obtained the charge density change ($\Delta\rho$) caused by the proton migrated from 6th water layer to nth water layer via the following Equation 3:

$$\Delta\rho = \left(\rho_{nth} - \rho^0_{nth}\right) - \left(\rho_{6th} - \rho^0_{6th}\right) \quad \text{(Equation 3)}$$

Here, the ρ_{nth} is the charge density of the proton at the nth water layer under the potential of −4.44 V. The ρ^0_{nth} is the charge density of the neutral system with protons at the nth water layer. The $(\rho_{nth} - \rho^0_{nth})$ can eliminate the errors caused by atoms' positions. The $(\rho_{6th} - \rho^0_{6th})$ is used as a reference. This allows us to locate the N_{ct} as shown in Figures 3C and 2D. When the proton migrates from the outer Helmholtz layers to the Pt (111) surface, the adiabatic transferred electron is mainly found in two locations: the interlayer between the electrode and water layer, and the oxygen framework of the first water layer. The intensity of these two peaks gradually increases when the proton migrates closely to the Pt (111) surface as implied by the Equation 2. Meanwhile, the sum of the electrons in these two peaks is about equal to the total obtained electrons shown in Figure 3A and Table S2 in the supplemental information. These electrons gather on the surfaces of the electrode during the proton migration and wait for the reduction process.

Based on the PDOS analysis of the H-1s and O-2p in the H_3O^+, and O-2p of water in the first water layer during the proton migration and reduction process as shown in Figure S2, supplemental information, No PDOS of H_3O^+ is shifted over the Fermi level during the proton migration. Thus, the proton is not reduced during the proton migration. However, induced by the negatively charged Pt electrode, there is a tiny PDOS of the first water layer's O-2p spanning across the Fermi level. Therefore, some electrons spillover to the oxygen in the first water layer during the proton migration.

The concerted proton-electron transfer mechanism facilitates the proton to overcome the chemical barrier in the migration pathway at the expense of the electrical energy carried by the transferred charge. The negative free energy change ($G_{n^{th},U_{abs}}$, see Equation S1 in supplemental information for details) can be used to describe the promotion of proton migration. In Figure 4A, we compare the grand free energy evolution during the proton migration and reduction processes under constant potentials ranging from −4.84 V to −4.24 V, as shown. Here, the $G_{6^{th},U_{abs}}$ is set to zero. Under the absolute potential of −4.84 V, the proton at the 6th water layer is 0.31V more stable than it is on the Pt (111) surface,

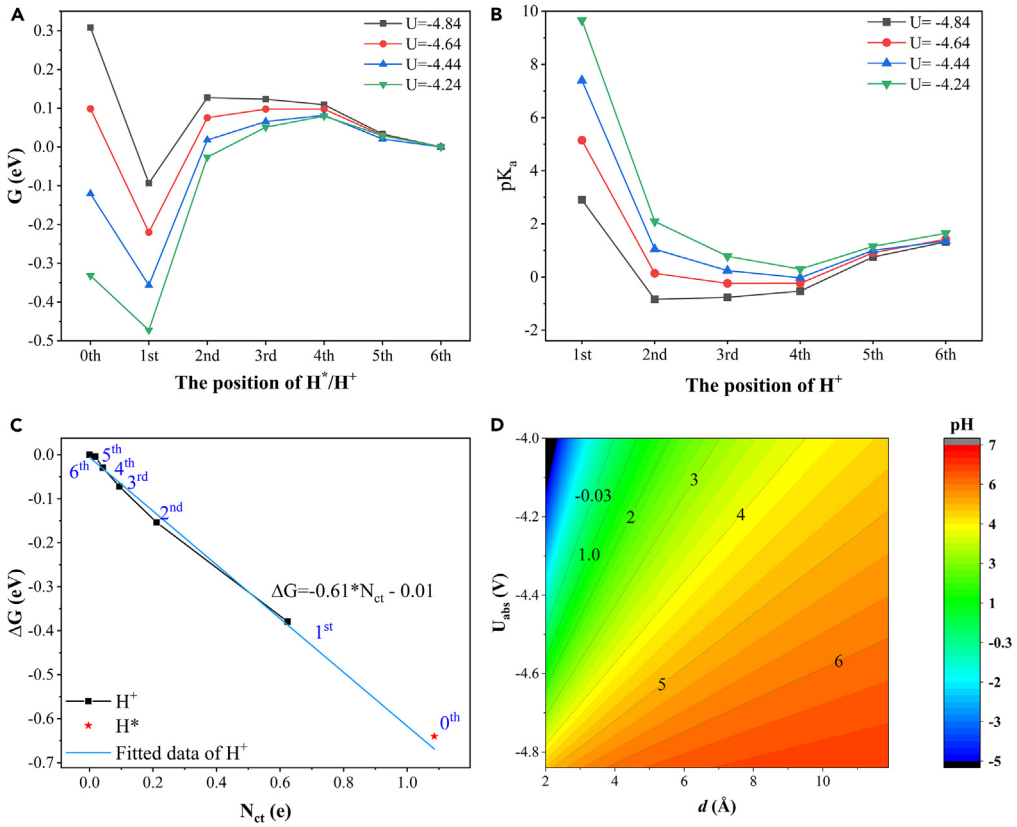

Figure 4. The grand free energy evolution during proton migration and reduction

(A) The grand free energy evolution during the whole proton migration step under several constant potentials; the grand free energy of the proton at the 6th water layer is set to zero; (B) the hydronium pK_a as a function of water layers and as a function of applied potential; (C) the grand free energy change from −4.84 V to −4.24 V as a function of the N_{ct} during the proton migration; the grand free energy change of the proton at the 6th water layer is set to zero. The grand free energy of H* on the Pt electrode is slightly deviating from the fitted data, which can be ascribed to the proton's chemical potential changing from H_2O-H to Pt-H and is not used as data for the fitting; (D) the local pH value as a function of U_{abs} of the electrode and its distance from the electrode. The pH of the bulk solvent is set to 7.

thus the hydrogen reduction is nonspontaneous. The electrode will get more negative charges which will stabilize the proton on the electrode as the the absolute potential rises. When the absolute potential increased to −4.44 V (0 V vs. SHE), the proton on the Pt surface is more stable than it in the 6th water layer by 0.12 eV, but is still unstable in comparison with the proton in the 1st water layer by 0.24 eV. Since the proton on the Pt surface and at the 1st water layer is energetically more favorable than that at the outer Helmholtz layer, more protons are expected to accumulate at the 1st water layer based on the Boltzmann distribution. The increased concentration of proton near the cathode will raise the protons' grand free energy, allowing the proton to overcome the shallow well and complete the reduction process. The free energy proton in the first water layer (−0.47 eV) and on the Pt surface (−0.33 eV) is more negative compared to it at the 6th water layer when the absolute potential is further increased to −4.24 V (−0.2 V vs. SHE). Therefore, the rise in the absolute potential promotes proton migration and hydrogen reduction processes.

Recasting the data in Figure 4A yields the hydronium pK_a as a function of water layers at various applied potentials. The predicted hydronium pK_a at the first water layer (pK_a = 2.9, 0.4 V vs. SHE) corroborates the experimental surface-specific electrical transport spectroscopy results (pK_a = 4.3) and the reactive force field molecular dynamics calculation (pK_a of 2.5–4.4).[23] A large hydronium pK_a indicates hydroniums enricher near the water layer and vice versa. As we can see, the hydronium pK_a at the sixth layer (and beyond) is unrelated to the potential, indicating that the electric field generated by the electrode has already decayed at the sixth layer. The hydronium pK_a decreases slightly at the 5th and 4th water layers, then rises dramatically at the closer water layers. The hydronium pK_a will rise with a higher applied potential, especially at closer water layers.

Based on the previous analysis, the promotion magnitude is sensitive to the absolute potential change, the proton's distance to the electrode, and the transferred charge, in which the transferred charge is related to the proton's distance to the electrode. In the following, we attempt to establish the functional relationship between the promotion magnitude, the absolute potential, and the transferred charge quantitatively. The promotion magnitude of the potential change from −4.84 V to −4.24 V is defined as:

$$\Delta G_{-4.84\ to\ -4.24} = G_{n^{th},-4.24} - G_{n^{th},-4.84} \quad \text{(Equation 4)}$$

Table S2 of supplemental information lists the N_{ct} of the proton in each water layer. Figure 4C shows the $\Delta G_{-4.24\ to\ -4.84}$ as a function of the N_{ct} during the proton migration. As we can see, the ΔG is negatively correlated with the N_{ct} of the proton migrating to the specific water-layer. The negative slope is fitted to be −0.61, which is close to the negative potential change (−4.84 to −4.24). Thus, the ΔG can be estimated by the Equation 5,

$$\Delta G = -N_{ct}\Delta U_{abs} \quad \text{(Equation 5)}$$

The N_{ct} is positive during the proton migration. The rise in U_{abs} will promote proton migration toward the electrode in the solvent (the energy-favorable locations), and the magnitude of this promotion is negatively proportional to the N_{ct} and the absolute potential, which explains the inhomogeneous distribution of protons in the electrical double layer.[24,25] In comparison with the outer Helmholtz layer, a higher absolute potential will induce a higher proton concentration near the electrode.

The relationship between absolute potential and proton concentration is estimated by the Boltzmann distribution equation which converts the ΔG into the proton distribution. It is reasonable to ignore the proton-proton interactions under the experimental proton concentration (Under pH = 0, for example, the proton concentration corresponds to one proton per 65 water molecules). Thus, the protons can be considered as distinguishable particles for the Boltzmann distribution equation. The local proton concentration or the local pH value should be sensitive to the ΔG, or the N_{ct} and absolute potential. Since there is no electric field in the electrical double layer to relocate the proton under the PZC, in both the inner and outer Helmholtz layers, the proton concentration is uniform and the ΔG is zero. Based on this assumption, the PZC is the reference potential for calculating the proton concentration difference between the inner/outer Helmholtz layer. The PZC can be estimated by the potential at which the grand free energy of the proton in the inner and outer Helmholtz is equal as given in Equations S3–S6, supplemental information. The calculated potential of the zero-charge potential of Pt (111) is −4.99 V (0.55 V vs. SHE) in this work, which is consistent with the experimental value (0.55 V vs. SHE).[26] Thus, the local proton concentration or the local pH value can be estimated by the U_{abs} of the electrode and the proton's distance from the electrode as present in Equation 6 (the derivation can be found in the supplemental information).

$$pH = pH_0 - \frac{1.66(U_{abs}+4.99)}{dkTln10} \quad \text{(Equation 6)}$$

Figure 4D illustrates the local pH calculated by Equation 6 when the pH of bulk solvent (pH_0) is 7. As we can see, the local pH value is negatively proportional to the U_{abs}, while it is inversely proportional to its distance from the cathode. Our results confirmed that the proton concentration in the electrical double layer is inhomogeneous, which is evidenced by the pH gradient observed in the continuous-flow Raman electrochemical cell.[25]

DISCUSSION

We reproduce the electrical double layer above the Pt (111) surface using a hybrid water solvent and the grand canonical fixed-potential approach. An electrostatic potential drop occurs at the boundary between the Pt electrode and water layers caused by the negatively charged electrode and positively charged water layers under the absolute potential of −4.44 V. The band alignment of the Pt surface and water layers is compatible with electrostatic potential drop. In the following, we track the electrons and grand free energy change of the entire system during the proton migration and reduction processes in the Volmer reaction. In doing so, we establish the relationship between transferred electrons, free energy, and potential for the first time. Our study has answered a few long-standing questions in this area: (1) the proton migration goes through the concerted proton-electron transfer mechanism, which overcomes the chemical barrier along the migration pathway at the cost of the electrical energy carried by the transferred charge; (2) the quantity of induced electron transfer from the external reservoir to the electrical double layer system is inversely proportional to the distance between the proton and electrode during the proton migration, which is accounting for more than half of the electrons and electrical energy involved in the Volmer reaction. Consequently, the proton migration in the electrical double layer is an essential component of the electrochemical reaction in terms of electron transfer and energy conversation; (3) the dissipated electrical energy reduces the chemical potential of the proton and induces the accumulation of proton near the negatively charged electrode. As a result, the local pH value is negatively proportional to the absolute potential and inversely proportional to its distance from the electrode. All these discoveries provide new insights for rational design and optimization of electrochemical systems.

Limitations of the study

It is worth noting that Equation 6 is a simple equation to convert the calculated data (the charge transfer and free energy evolution during the proton migration) to the local proton concentration observed in the experiment under various applied potentials. We admit that there are many factors, like electrode voltage, the concentration of other ions, proton concentration, and H* coverage, that are not considered in this model. All these factors will alter the local free energy profile of the proton in the solvent slightly, and bring a small derivation to Equation 6. An exact energy evolution profile does need to account for all local environmental variables, which is beyond theoretical and experimental capability at the present stage.

STAR★METHODS

Detailed methods are provided in the online version of this paper and include the following:

- KEY RESOURCES TABLE
- RESOURCE AVAILABILITY
  - Lead contact
  - Materials availability
  - Data and code availability
- METHOD DETAILS
- QUANTIFICATION AND STATISTICAL ANALYSIS
- ADDITIONAL RESOURCES

SUPPLEMENTAL INFORMATION

Supplemental information can be found online at https://doi.org/10.1016/j.isci.2023.108318.

ACKNOWLEDGMENTS

This work was supported by the "Young Talent Support Plan" of Xi'an Jiaotong University (grant no. 11304222010715), the Shaanxi Province Merit-based Overseas Scholars Funding for Scientific and Technological Activities (grant no. 2022-13), and the National Natural Science Foundation of China (NSFC) (grant no. 22303063). The theoretical work in this research used the resources of the Mcloud High-Performance Computing supported by the Longxun Quantum.

AUTHOR CONTRIBUTIONS

G.G. and L.-W.W. conceived the concept and developed the model. G.G.carried out the calculations, and wrote the paper. Both authors discussed the results and commented on the paper.

DECLARATION OF INTERESTS

The authors declare no competing interests.

Received: April 4, 2023
Revised: August 3, 2023
Accepted: October 20, 2023
Published: October 29, 2023

REFERENCES

1. Gao, G., and Wang, L.-W. (2021). A potential and pH inclusive microkinetic model for hydrogen reactions on Pt surface. Chem Catal. *1*, 1331–1345. https://doi.org/10.1016/j.checat.2021.10.006.
2. Gao, G., Jiao, Y., Waclawik, E.R., and Du, A. (2016). Single Atom (Pd/Pt) Supported on Graphitic Carbon Nitride as an Efficient Photocatalyst for Visible-Light Reduction of Carbon Dioxide. J. Am. Chem. Soc. *138*, 6292–6297. https://doi.org/10.1021/jacs.6b02692.
3. Honkala, K., Hellman, A., Remediakis, I.N., Logadottir, A., Carlsson, A., Dahl, S., Christensen, C.H., and Nørskov, J.K. (2005). Ammonia Synthesis from First-Principles Calculations. Science *307*, 555–558. https://doi.org/10.1126/science.1106435.
4. Nørskov, J.K., Rossmeisl, J., Logadottir, A., Lindqvist, L., Kitchin, J.R., Bligaard, T., and Jónsson, H. (2004). Origin of the Overpotential for Oxygen Reduction at a Fuel-Cell Cathode. J. Phys. Chem. B *108*, 17886–17892. https://doi.org/10.1021/jp047349j.
5. Qiao, J., Liu, Y., Hong, F., and Zhang, J. (2014). A review of catalysts for the electroreduction of carbon dioxide to produce low-carbon fuels. Chem. Soc. Rev. *43*, 631–675. https://doi.org/10.1039/C3CS60323G.
6. Lin, S., Diercks, C.S., Zhang, Y.-B., Kornienko, N., Nichols, E.M., Zhao, Y., Paris, A.R., Kim, D., Yang, P., Yaghi, O.M., and Chang, C.J. (2015). Covalent organic frameworks comprising cobalt porphyrins for catalytic CO_2 reduction in water. Science *349*, 1208–1213. https://doi.org/10.1126/science.aac8343.
7. Jiao, Y., Zheng, Y., Jaroniec, M., and Qiao, S.Z. (2015). Design of electrocatalysts for oxygen- and hydrogen-involving energy conversion reactions. Chem. Soc. Rev. *44*, 2060–2086. https://doi.org/10.1039/C4CS00470A.
8. Quaino, P., Luque, N.B., Soldano, G., Nazmutdinov, R., Santos, E., Roman, T., Lundin, A., Groß, A., and Schmickler, W. (2013). Solvated protons in density functional theory—A few examples. Electrochim. Acta *105*, 248–253. https://doi.org/10.1016/j.electacta.2013.04.084.
9. Chen, L.D., Bajdich, M., Martirez, J.M.P., Krauter, C.M., Gauthier, J.A., Carter, E.A., Luntz, A.C., Chan, K., and Nørskov, J.K. (2018). Understanding the apparent fractional charge of protons in the aqueous electrochemical double layer. Nat. Commun. *9*, 3202. https://doi.org/10.1038/s41467-018-05511-y.
10. Gao, G., and Wang, L.W. (2020). Substantial potential effects on single-atom catalysts for the oxygen evolution reaction simulated via a fixed-potential method. J. Catal. *391*, 530–538. https://doi.org/10.1016/j.jcat.2020.08.032.
11. Ringe, S., Hörmann, N.G., Oberhofer, H., and Reuter, K. (2022). Implicit Solvation Methods for Catalysis at Electrified Interfaces. Chem. Rev. *122*, 10777–10820. https://doi.org/10.1021/acs.chemrev.1c00675.
12. Liu, C., Qian, J., Ye, Y., Zhou, H., Sun, C.-J., Sheehan, C., Zhang, Z., Wan, G., Liu, Y.-S., Guo, J., et al. (2020). Oxygen evolution reaction over catalytic single-site Co in a well-defined brookite TiO_2 nanorod surface. Nat. Catal. *4*, 36–45. https://doi.org/10.1038/s41929-020-00550-5.
13. Song, J., Kwon, S., Hossain, M.D., Chen, S., Li, Z., and Goddard, W.A. (2021). Reaction Mechanism and Strategy for Optimizing the Hydrogen Evolution Reaction on Single-Layer 1T′ WSe_2 and WTe_2 Based on Grand Canonical Potential Kinetics. ACS Appl. Mater. Interfaces *13*, 55611–55620. https://doi.org/10.1021/acsami.1c14234.

14. Huang, Y., Nielsen, R.J., and Goddard, W.A., III (2018). Reaction Mechanism for the Hydrogen Evolution Reaction on the Basal Plane Sulfur Vacancy Site of MoS_2 Using Grand Canonical Potential Kinetics. J. Am. Chem. Soc. *140*, 16773–16782. https://doi.org/10.1021/jacs.8b10016.
15. Hu, X., Chen, S., Chen, L., Tian, Y., Yao, S., Lu, Z., Zhang, X., and Zhou, Z. (2022). What is the Real Origin of the Activity of Fe–N–C Electrocatalysts in the O_2 Reduction Reaction? Critical Roles of Coordinating Pyrrolic N and Axially Adsorbing Species. J. Am. Chem. Soc. *144*, 18144–18152. https://doi.org/10.1021/jacs.2c08743.
16. Zhao, X., and Liu, Y. (2021). Origin of Selective Production of Hydrogen Peroxide by Electrochemical Oxygen Reduction. J. Am. Chem. Soc. *143*, 9423–9428. https://doi.org/10.1021/jacs.1c02186.
17. Sundararaman, R., and Ping, Y. (2017). First-principles electrostatic potentials for reliable alignment at interfaces and defects. J. Chem. Phys. *146*, 104109. https://doi.org/10.1063/1.4978238.
18. Cheng, J., and Sprik, M. (2014). The electric double layer at a rutile TiO_2 water interface modelled using density functional theory based molecular dynamics simulation. J. Phys. Condens. Matter *26*, 244108. https://doi.org/10.1088/0953-8984/26/24/244108.
19. Fisicaro, G., Genovese, L., Andreussi, O., Marzari, N., and Goedecker, S. (2016). A generalized Poisson and Poisson-Boltzmann solver for electrostatic environments. J. Chem. Phys. *144*, 014103. https://doi.org/10.1063/1.4939125.
20. Trasatti, S. (1986). The absolute electrode potential: an explanatory note (Recommendations 1986). Pure Appl. Chem. *58*, 955–966. https://doi.org/10.1351/pac198658070955.
21. Booth, F. (1951). The Dielectric Constant of Water and the Saturation Effect. J. Chem. Phys. *19*, 391–394. https://doi.org/10.1063/1.1748233.
22. El-Hag, A., Zheng, Z., Boggs, S.A., and Jayaram, S. (2005). Effect of dielectric saturation of water on transmembrane potential in biological cells. IEEE Int. Conf. Dielectr. Liq. 453–456. https://doi.org/10.1109/ICDL.2005.1490123.
23. Zhong, G., Cheng, T., Shah, A.H., Wan, C., Huang, Z., Wang, S., Leng, T., Huang, Y., Goddard, W.A., and Duan, X. (2022). Determining the hydronium pKa; at platinum surfaces and the effect on pH-dependent hydrogen evolution reaction kinetics. Proc. Natl. Acad. Sci. USA *119*, e2208187119. https://doi.org/10.1073/pnas.2208187119.
24. Stern, O. (1924). Zur theorie der elektrolytischen doppelschicht. Z. Elektrochem. Angew. Phys. Chem. *30*, 508–516. https://doi.org/10.1002/bbpc.192400182.
25. Lu, X., Zhu, C., Wu, Z., Xuan, J., Francisco, J.S., and Wang, H. (2020). In Situ Observation of the pH Gradient near the Gas Diffusion Electrode of CO_2 Reduction in Alkaline Electrolyte. J. Am. Chem. Soc. *142*, 15438–15444. https://doi.org/10.1021/jacs.0c06779.
26. Iwasita, T., and Xia, X. (1996). Adsorption of water at Pt(111) electrode in $HClO_4$ solutions. The potential of zero charge. J. Electroanal. Chem. *411*, 95–102. https://doi.org/10.1016/0022-0728(96)04576-7.
27. Jia, W., Cao, Z., Wang, L., Fu, J., Chi, X., Gao, W., and Wang, L.-W. (2013). The analysis of a plane wave pseudopotential density functional theory code on a GPU machine. Comput. Phys. Commun. *184*, 9–18. https://doi.org/10.1016/j.cpc.2012.08.002.
28. Perdew, J.P., Burke, K., and Ernzerhof, M. (1996). Generalized Gradient Approximation Made Simple. Phys. Rev. Lett. *77*, 3865–3868.
29. Perdew, J.P., Ernzerhof, M., and Burke, K. (1996). Rationale for mixing exact exchange with density functional approximations. J. Chem. Phys. *105*, 9982–9985. https://doi.org/10.1063/1.472933.
30. Grimme, S. (2006). Semiempirical GGA-type density functional constructed with a long-range dispersion correction. J. Comput. Chem. *27*, 1787–1799. https://doi.org/10.1002/jcc.20495.
31. Wang, Z., Yang, Y., Olmsted, D.L., Asta, M., and Laird, B.B. (2014). Evaluation of the constant potential method in simulating electric double-layer capacitors. J. Chem. Phys. *141*, 184102. https://doi.org/10.1063/1.4899176.
32. Goodpaster, J.D., Bell, A.T., and Head-Gordon, M. (2016). Identification of Possible Pathways for C–C Bond Formation during Electrochemical Reduction of CO_2: New Theoretical Insights from an Improved Electrochemical Model. J. Phys. Chem. Lett. *7*, 1471–1477. https://doi.org/10.1021/acs.jpclett.6b00358.
33. Letchworth-Weaver, K., and Arias, T.A. (2012). Joint density functional theory of the electrode-electrolyte interface: Application to fixed electrode potentials, interfacial capacitances, and potentials of zero charge. Phys. Rev. B *86*, 075140. https://doi.org/10.1103/PhysRevB.86.075140.
34. Melander, M.M., Kuisma, M.J., Christensen, T.E.K., and Honkala, K. (2019). Grand-canonical approach to density functional theory of electrocatalytic systems: Thermodynamics of solid-liquid interfaces at constant ion and electrode potentials. J. Chem. Phys. *150*, 041706. https://doi.org/10.1063/1.5047829.
35. Lindgren, P., Kastlunger, G., and Peterson, A.A. (2020). A Challenge to the G ~ 0 Interpretation of Hydrogen Evolution. ACS Catal. *10*, 121–128. https://doi.org/10.1021/acscatal.9b02799.
36. Kastlunger, G., Lindgren, P., and Peterson, A.A. (2018). Controlled-Potential Simulation of Elementary Electrochemical Reactions: Proton Discharge on Metal Surfaces. J. Phys. Chem. C *122*, 12771–12781. https://doi.org/10.1021/acs.jpcc.8b02465.
37. Mathew, K., Sundararaman, R., Letchworth-Weaver, K., Arias, T.A., and Hennig, R.G. (2014). Implicit solvation model for density-functional study of nanocrystal surfaces and reaction pathways. J. Chem. Phys. *140*, 084106. https://doi.org/10.1063/1.4865107.
38. Nie, S., Feibelman, P.J., Bartelt, N.C., and Thürmer, K. (2010). Pentagons and Heptagons in the First Water Layer on Pt(111). Phys. Rev. Lett. *105*, 026102. https://doi.org/10.1103/PhysRevLett.105.026102.
39. Roman, T., and Groß, A. (2013). Structure of water layers on hydrogen-covered Pt electrodes. Catal. Today *202*, 183–190. https://doi.org/10.1016/j.cattod.2012.06.001.
40. Wang, Y.-H., Zheng, S., Yang, W.-M., Zhou, R.-Y., He, Q.-F., Radjenovic, P., Dong, J.-C., Li, S., Zheng, J., Yang, Z.-L., et al. (2021). In situ Raman spectroscopy reveals the structure and dissociation of interfacial water. Nature *600*, 81–85. https://doi.org/10.1038/s41586-021-04068-z.
41. Gonella, G., Backus, E.H.G., Nagata, Y., Bonthuis, D.J., Loche, P., Schlaich, A., Netz, R.R., Kühnle, A., McCrum, I.T., Koper, M.T.M., et al. (2021). Water at charged interfaces. Nat. Rev. Chem *5*, 466–485. https://doi.org/10.1038/s41570-021-00293-2.
42. Bartlett, P.N., and Cook, D.A. (2015). Measurements of the double layer capacitance for electrodes in supercritical CO_2/acetonitrile electrolytes. J. Electroanal. Chem. *746*, 18–24. https://doi.org/10.1016/j.jelechem.2015.03.022.
43. Pajkossy, T., and Kolb, D.M. (2001). Double layer capacitance of Pt(111) single crystal electrodes. Electrochim. Acta *46*, 3063–3071. https://doi.org/10.1016/S0013-4686(01)00597-7.
44. Sibert, E., Faure, R., and Durand, R. (2001). High frequency impedance measurements on Pt(111) in sulphuric and perchloric acids. J. Electroanal. Chem. *515*, 71–81. https://doi.org/10.1016/S0022-0728(01)00639-8.

STAR★METHODS

KEY RESOURCES TABLE

REAGENT or RESOURCE	SOURCE	IDENTIFIER
Software and algorithms		
PWmat	Jia et al.[27]	http://www.pwmat.com/
Python version 2.7	Python Software Foundation	https://www.python.org

RESOURCE AVAILABILITY

Lead contact

Further information and requests for resources and Softwares should be directed to and will be fulfilled by the lead contact, Dr. Guoping Gao (guopinggao@xjtu.edu.cn).

Materials availability

This study did not use any reagents.

Data and code availability

- The published article includes all datasets generated or analyzed during this study.
- This paper does not report original code.
- Any additional information required to reanalyze the data reported in this paper is available from the lead contact upon request.

METHOD DETAILS

All calculations were performed using planewave DFT calculations implemented in the PWmat code with norm-conserving SG15 pseudopotential.[27] The exchange-correlation interactions were treated by the generalized gradient approximation in the form of the Perdew–Burke–Ernzerhof functional.[28,29] The Van der Waals interaction was described by using the empirical correction in Grimme's scheme, i.e. DFT+D_3.[30] The electron wave functions were expanded by plane waves with cut-off energies of 680 eV, and the convergence tolerance for residual force and energy on each atom during structure relaxation were set to 0.005 eV $Å^{-1}$ and 10^{-5} eV, respectively. The Brillouin zone was sampled with the Monkhorst−Pack K-point mesh of 3×3×1. A linearized Poisson-Boltzmann equation[19] is used to screen the ions' electrostatic potential exponentially in the implicit solvent zone and provide a converged flat potential far away from the surface. The flat potential provides a reference potential to fix the electrode potential and to compare with the experiment. All the calculations are done under the scheme of the fixed-potential method, in which the total charge of the system is automatically adjusted for a given potential.[31,32]

Several groups have recently developed DFT-based fixed-potential (or constant-potential) methods for electrochemical simulation.[32,33] In these methods, an outside loop of an existing *ab initio* package (e.g., PWSCF and GPAW) was used to adjust the total electron of the system until the desired Fermi energy is reached as summarized in the left panel of Figure 1. For the PWSCF or GPAW to realize structure optimization under constant potential, each or a few ionic steps are followed by a potential-equilibration step, in which the amount of electrons is adjusted to ensure the potential is within tolerance.[34–36] The drawbacks of these approaches include being computationally expensive and ignoring the correlations between charge and the structures, which prevent people from performing complex calculations, including NEB and *ab initio* MD under constant potential. Here, the fixed-fermi-energy self-consistent field (SCF) procedure is embedded in the DFT electronic structure calculation itself, which can significantly speed up the calculation without the use of the outside loop. Additionally, our fixed-potential technique enables atomic relaxation (Figure 1A), NEB (Figure 1B), and *ab initio* MD (Figure 1C) at a given constant potential U. All these functions are implemented in the PWmat software.

The Pt (111) electrode is modeled with a p (3x3) and 4-layer slab with the inner two layers of Pt fixed. The two Pt(111) surfaces are terminated by 5/9 monolayers of H* as suggested by our previous work.[1] To simulate the microchemical environment of the solid-solvent interface, each Pt (111) surface is covered with a six-water-layers in mirror symmetry (see Figures 2A–2D). The vacuum region beyond the explicit water layers, which is ~16 Å along the Z-direction, is simulated by the implicit solvent model.[37] A hexagonal H_2O-molecule lattice, which is commensurate with the substrate Pt (111) lattice, is found on the Pt (111) surface in the experiment.[38,39] The recent Raman spectra of interfacial water also reveal that the interfacial waters are highly organized under the hydrogen evolution reaction potentials.[40,41] Therefore, hexagonal water layers with 'two-H-down and one-H-up' configurations under the ABC arrangement, rather than random and highly fluctuating water clusters above Pt (111), are used in our work. To minimize the back-interface of the Pt electrode's effects, we construct a symmetric Pt slab electrode with water and proton migrations on both sides of the electrode. The high symmetry of our model can improve the convergency in the charge transfer and energy exchange calculations.

To simulate the different stages of proton migration and the reduction process, one excess proton at each side of Pt (111) is added symmetrically to the different water layers and Pt (111) sequentially. At the potential of U=-4.44 V, the (3x3) supercell of Pt(111) unit cell

with six-water layer has a capacitance of 26.80 μF/cm^2, which is consistent with the value of the (6x6) supercell (26.74 μF/cm^2, see Figure S8 in supplemental information), and is in reasonable agreement with the experimental value of 9-38 μF/cm^2.[42–44]

QUANTIFICATION AND STATISTICAL ANALYSIS

Results are presented as either absolute values or mean +/− standard deviation, with the sample number n stated wherever relevant.

ADDITIONAL RESOURCES

Does not apply.